IET Image Processing

*Research Article*

IET Journals
The Institution of Engineering and Technology

# Improved automated detection of glaucoma from fundus image using hybrid structural and textural features

ISSN 1751-9659
Received on 3rd October 2016
Revised 3rd May 2017
Accepted on 14th May 2017
E-First on 8th August 2017
doi: 10.1049/iet-ipr.2016.0812
www.ietdl.org

*Tehmina Khalil[1], Muhammad Usman Akram[2] ✉, Samina Khalid[1], Amina Jameel[3]*

[1]*Department of Software Engineering, Bahria University Islamabad, Islamabad, Pakistan*
[2]*Department of Computer Engineering, College of E&ME, National university of Sciences & Technology, Islamabad, Pakistan*
[3]*Department of Computer Engineering, Bahria University Islamabad, Islamabad, Pakistan*
✉ *E-mail: usmakram@gmail.com*

**Abstract:** Glaucoma is a group of eye disorders that damage the optic nerve. Considering a single eye condition for the diagnosis of glaucoma has failed to detect all glaucoma cases accurately. A reliable computer-aided diagnosis system is proposed based on a novel combination of hybrid structural and textural features. The system improves the decision-making process after analysing a variety of glaucoma conditions. It consists of two main modules hybrid structural feature-set (HSF) and hybrid texture feature-set (HTF). HSF module can classify a sample using support vector machine (SVM) from different structural glaucoma condition and the HTF module analyses the sample founded on various texture and intensity-based features and again using SVM makes a decision. In the case of any conflict in the results of both modules, a suspected class is introduced. A novel algorithm to compute the super-pixels has also been proposed to detect the damaged cup. This feature alone outperformed the current state-of-the-art methods with 94% sensitivity. Cup-to-disc ratio calculation method for cup and disc segmentation, involving two different channels has been introduced increasing the overall accuracy. The proposed system has given exceptional results with 100% accuracy for glaucoma referral.

## 1 Introduction

Glaucoma is a painless neurological disease which is hard to diagnose especially in the early stages due to a very slow progression rate. The World Health Organization (WHO) has labelled it as the second most prevalent cause of blindness worldwide. There is a huge increment in glaucoma patients every year; the estimated number of possible glaucoma patients worldwide in the forthcoming decades has shown frightening escalation. It is estimated that ∼60 million individuals currently suffer from blindness globally due to glaucoma [1] and this figure will further increase to 76 million by 2020 [2]. Glaucoma is a group of eye diseases that have common conducts such as elevated intraocular pressure, damage to optic nerve head, gradual vision loss and ultimately blindness. Glaucoma diagnosis is a clinical diagnosis since it cannot be detected with blood or definite genetic test. Diagnosis in the early period is very crucial to prevent blindness; hence, regular screening of patient can aid in diagnosing disease at an early and treatable stage. Existing pre-diagnosis is invasive, expensive and time consuming; therefore, computer-aided diagnosis (CAD) of glaucoma may become a game changer in the coming years. The CAD is simple, repetitive, exceptionally fast in the diagnosis and free from inter- and intra-observer variability. The CAD can be very helpful in developing countries where there is a scarcity of ophthalmologist as it can bring the clinician to the level of an expert observer.

Fundoscopy is capable of capturing objective, accurate and precise quantitative information about optic nerve and retinal structure. Optic disc (OD) is a point on the retina where the optic nerve leaves the eye. Visual information is transmitted through fibre nerves present in the optic nerve to the brain. In glaucoma, decay of fibre nerves cause cup size to increase and as a result cup-to-disc ratio (CDR) also increases. The CDR value ≤to 0.5 is considered as normal whereas >0.5 is considered as glaucomatous. In initial and intermediate stage of glaucoma, the vertical CDR increases rapidly [3]. One way to quantify this disease is by considering CDR and other structural features of the retina; however, another way is by assessing the overall appearance and texture of the retinal image.

Automated glaucoma diagnosis is one of the vibrant research fields in biomedical imaging. Many image processing and machine learning techniques have been applied to come up with more accurate results. A recent study has used sparse dissimilarity constrained technique for CDR calculation with 88% accuracy [4]. Super intensity pixel based CDR calculations achieved 90% accuracy [5]. Thresholding and counting white pixels to calculate CDR along with ISNT (inferior < superior < nasal < temporal) rules for detection gained 94% accuracy [6]. In [7], threshold values have been derived by performing statistical analysis of histogram to segment cup and disc. Vessel bends for cup and disc detection accomplished 88% accuracy [8]. Canny edge detector and thresholding was applied on vessel free image to detect cup and disc boundaries and attained 85% accuracy [9]. Similarly, the overall appearance of the image has also been involved in automated diagnosis of glaucoma, in a recent research various texture features have been extracted using Gabor transformation and achieved 93% accuracy using support vector machine (SVM) classifier [10]. Two-dimensional (2D) discrete wavelet transform (DWT) has been used to calculate texture features and attained a total of 93% accuracy using SVM classifier in [11]. Global image information has been extracted using an extension of generalised moment pattern. PCA-DD classifier has been used, and 94% accuracy has been gained in [12].

Our proposed novel system achieved 100% accuracy for glaucoma referral. The prime innovation of proposed system lies in the formation of two distant, versatile and hybrid features set used in the detection process. In addition, a novel algorithm to compute regular, compact super-pixels calculation with low computational overhead is proposed. Our unique super-pixel calculation algorithm outperformed other current state-of-the-art methods with 94% sensitivity. Also, a new CDR calculation method has been introduced to accomplish high accuracy rate in CAD system by involving two different colour channels for cup and disc segmentation.

The outline of the paper is as follows. Section 2 gives precise detail of proposed methodology. Section 3 explains different structural features involved in hybrid structural feature-set (HSF) module. Section 4 describes various textural and intensity-based

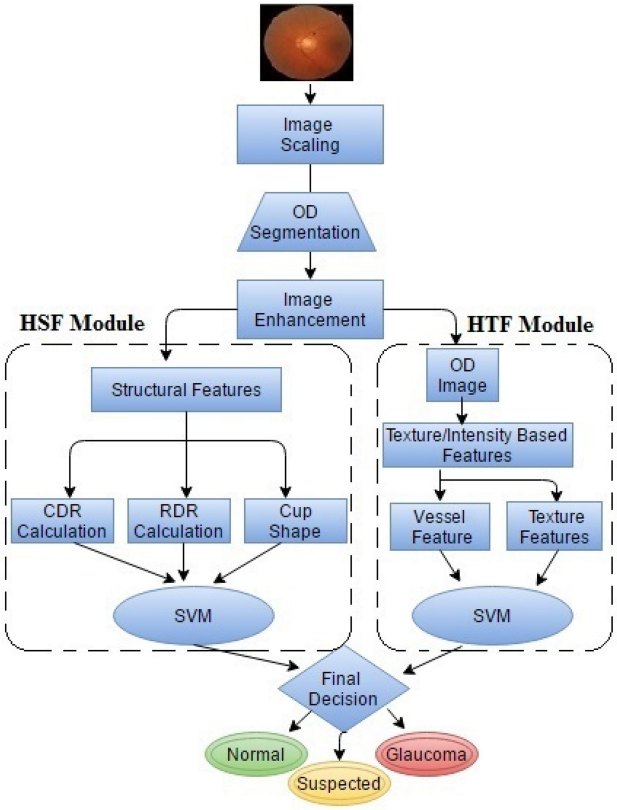


**Fig. 1** *Overview of proposed system architecture*

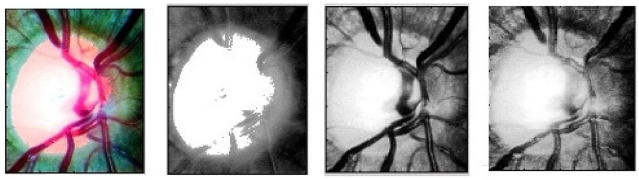


**Fig. 2** *Enh image after histogram equalisation*
***(a)*** Enh image, ***(b)*** Red channel of Enh image, ***(c)*** Green channel of Enh image, ***(d)*** Blue channel of Enh image

features included in hybrid texture feature-set (HTF) module. Section 5 describes imaging databases, experimental setup, and Section 6 gives results. The paper concludes in Section 7.

## 2 Proposed methodology

HSF and HTF are the two core modules of the proposed system. The HSF module further includes CDR computation, vertical rim-to-disc ratio (RDR) calculation and cup shape analysis from the enhanced (Enh) image. Three structural features () are calculated and used for classification in HSF module. Whereas, HTF module consists of two sub-modules; first sub-module includes rim vessel extraction and computation of texture features from extracted rim vessels and second sub-module consists of the formation of feature set based on texture and intensity-based features extracted from automatically cropped OD part of Enh image. In HTF module overall 115 texture and intensity based features ($f_4$–$f_{118}$) has been extracted for classification. Both modules use SVM along with radial basis function (RBF) for classification. Results from HSF and HTF module are correlated to make a final decision. The final determination also $f_1$–$f_3$includes a third class known as suspected class. If results of both modules do not converge on a single decision than sample is classified as suspected. Fig. 1 depicts the complete methodology.

Fundus image has been pre-processed before structural and texture feature extraction for better results. Spatial resolution has been improved using bilinear interpolation technique [13]. After image scaling, OD segmentation has been done [14]. Histogram equalisation technique has been employed to increase the contrast of cropped image [15]. The purpose of pre-processing is to cater images acquired from different fundus camera having different resolutions. In pre-processing, all input images are scaled and region of interest of size $200 \times 250$ containing OD is cropped. Fig. 2*a* shows Enh image after histogram equalisation.

## 3 HSF module

### *3.1 CDR calculation ($f_1$)*

CDR is one of the main clinical indicators involved in glaucoma diagnosis [16]. In glaucoma, due to decay of fibre nerves the cup size increases causing a significant difference between CDR value of glaucomatous and healthy eye. The CDR value >0.5 indicates glaucoma effected eye [3]. The complete process of proposed CDR calculation involving two different colour channels for cup and disc segmentation is described in Fig. 3.

*3.1.1 Disc segmentation:* We applied mean, median and Otsu's thresholding methods for cup and disc segmentation but we obtained best fits for OD segmentation using thresholding value $T = 0.4$. Fig. 2*b* represents red channel of Enh image, as it can be seen that red channel gives maximum visibility of disc, which makes it the most suitable channel for disc segmentation. Likewise, in disc segmentation process the binary image obtained after thresholding red channel is displayed in Fig. 4*c*. The imperfections encountered in the binary image after thresholding has been removed using morphological opening [17]. Fig. 4*d* shows image after morphological opening, and it can be observed that after morphological opening all small objects creating noise around OD are removed, and it also makes disc boundary smooth. Moreover, the opening will also open up gaps between large noisy objects around the disc, and all those large noisy objects having an area smaller than 20,000 pixels have been further removed [18]. Fig. 4*e* shows pure disc area after removing all noisy objects. Convex hull methodology has been applied to compute total area of the disc. After noise removal, only relevant bright pixels participating in disc area are left. Calculating convex hull will include all bright parts into single disc area and also fills any holes or unfilled portion as shown in Fig. 4*f*. Finally, canny edge detector has been used to identify the boundary of extracted disc area. The accuracy of extracted boundary is verified by plotting it on the original boundary as shown in Fig. 4*g*. Vertical length of the disc has been computed using 'Bounding Box' [19]. The bounding box is then plotted in Fig. 4*h* to visualise the accuracy of estimated vertical length of disc.

*3.1.2 Cup segmentation:* Blue channel of Enh image has been used for cup segmentation. Blue channel generated the maximum visualisation of the cup as shown in Fig. 2*d*. In blue channel, most of the blood vessels automatically merge into cup area, making it appropriate for error free cup segmentation. Thresholding blue channel of Enh image using threshold value $T = 0.9$, a binary image as shown in Fig. 5*c* has been obtained during cup segmentation. The salt noise has often been encountered in extreme corners of the binary image after thresholding. Therefore, the salt noise has been removed using minimum filter. Morphological closing using a large circular structuring element has been used to combine all remaining bright pixels into the single cup area as shown in Fig. 5*d*. After morphological closing, all connected objects smaller than 5000 pixels have been removed. Convex hull has been used to calculate total cup area as shown in Fig. 5*e*. Canny edge detector is applied to find boundaries of extracted cup area and derived cup boundaries are plotted on original image as shown in Fig. 5*f*. 'Bounding box' has been used to compute the vertical diameter of the cup, 'bounding box' capturing cup area is plotted in Fig. 5*g*.

*3.1.3 Cup-to-disc ratio:* The CDR has been calculated by taking the percentage of cup vertical diameter (CVD) to the disc vertical diameter (DVD) as described in the following equation:

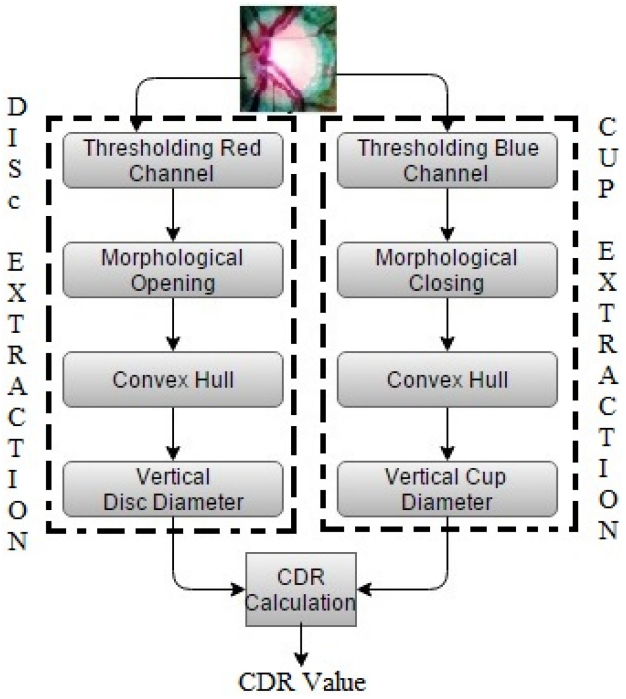


**Fig. 3** *CDR calculation flowchart*

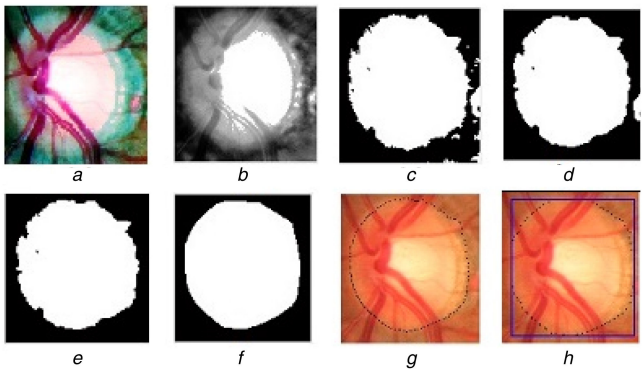


**Fig. 4** *Binary image obtained after thresholding red channel*
***(a)*** Enh image, ***(b)*** Red channel of Enh image, ***(c)*** Thresholding, ***(d)*** Morphological opening, ***(e)*** Large noisy objects removal, ***(f)*** Convex hull, ***(g)*** Disc boundary detection, ***(h)*** Vertical diameter

$$\mathrm{CDR} = \frac{\mathrm{CVD}}{\mathrm{DVD}} \tag{1}$$

### 3.2 Vertical RDR calculation ($f_2$)

The neuro-retinal rim (NRR) is the area between cup and disc boundary that contains axons of fibre nerve. In glaucoma, the degeneration of fibre nerves imposes rim size to decrease. The first fibre nerves effected by glaucoma are in the superior and inferior region of NRR [3]. The inferior is the bottommost region of NRR, whereas superior is the topmost region of NRR. In our case, we have computed vertical NRR (VNRR) which is the thickness of superior part of rim only, and it is computed by taking the difference of upper $y$-coordinates of cup and disc bounding box. Similarly, RDR is calculated by taking the ratio of VNRR to the DVD as described in (2). It is distinguishable from CDR value as a decrease in RDR value signifies glaucoma. In some cases, where CDR values fail to generate accurate classification results, RDR values can play a substantial role by analysing thickness of superior region. RDR value <0.1 is considered as glaucomatous [20]. Since the decrease in VNRR is one of the signs of glaucoma [21], hence we have used RDR as an indicator of glaucoma in HSF module

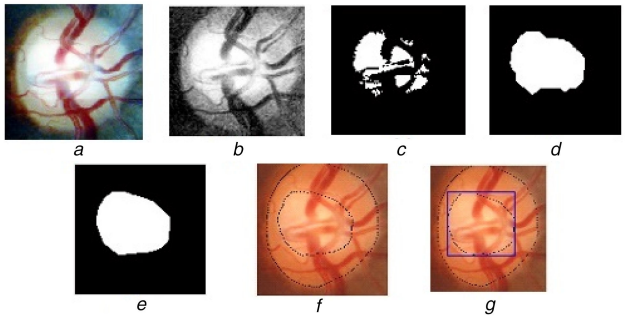


**Fig. 5** *Binary image obtained during cup segmentation*
***(a)*** Enh image, ***(b)*** Blue channel of Enh image, ***(c)*** Thresholding blue channel, ***(d)*** Morphological closing, ***(e)*** Computing convex hull, ***(f)*** Cup boundary detection, ***(g)*** Vertical cup diameter

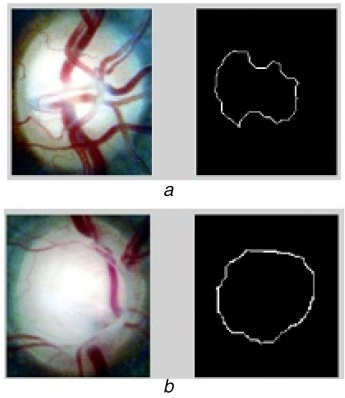


**Fig. 6** *Extracted cup contour of normal and glaucoma eye*
***(a)*** Normal eye's cup contour, ***(b)*** Glaucoma eye's cup contour

$$\mathrm{RDR} = \frac{\mathrm{VNRR}}{\mathrm{DVD}} \tag{2}$$

### 3.3 Cup shape analysis ($f_3$)

Fractal analysis can be used for classification of medical images on the base of regularity and irregularity of the contour of specific objects [22]. One of the early symptoms for glaucoma diagnosis involves changes in the cup shape, and in initial stages, it has been found that glaucoma causes changes in the cup shape due to movement of vessels, and it is more regular in glaucoma eye whereas in the normal eye it is more irregular. Similarly, fractal dimension for glaucoma eye is smaller due to its regular shape whereas it is greater for normal eye due to more irregular shape [23]. Hausdorff's dimension is one of the primary approaches used to find fractal dimension. In the proposed solution, Hausdorff's fractal dimension of cup contour has been calculated to analyse cup shape. Cup boundary extraction has been achieved by the erosion of extracted cup (Fig. 5*d*) and then subtraction of eroded cup from initially extracted cup area. Figs. 6*a* and *b* shows extracted cup contour of normal and glaucoma eye, respectively.

Considering an object that has Euclidean dimension $E$, the Hausdorff's fractal dimension $D_0$ can be computed by the following expression:

$$D_0 = \lim_{\epsilon \to 0} \frac{\log N(\epsilon)}{\log \epsilon^{-1}} \tag{3}$$

where $N(\epsilon)$ is the counting of hyper-cubes of dimension $E$ and length $\epsilon$ that fill the object.

Hausdorff's dimension calculation algorithm [24] used in proposed methodology can be described as following:

*Step 1:* Pad the segmented cup contour image (Fig. 6) with background pixels so that its dimensions are a power of 2.
*Step 2:* Set the box size ' $\epsilon$' to the size of the image.

*Step 3:* Compute $N(\epsilon)$, which corresponds to the number of boxes of size '$E$' which contains at least one object pixel.
*Step 4:* If $\epsilon - > 1$ then $\epsilon = \epsilon - /2$ and repeat step 3.
*Step 5:* Compute the points $\log(N(\epsilon)) \times \log(1/\epsilon)$ and use the least squares method to fit a line to the points.
*Step 6:* The returned Hausdorff's fractal dimension $D$ is the slope of the line.

The fractal dimension values found to be in range of 1.11–1.15 for glaucoma eye and for normal eye the range was 1.16–1.25.

## 4 HTF module

### 4.1 Rim vessels extraction ($f_4$–$f_9$)

Vascular changes can be one of the early indicators of glaucoma [25]. Vascular changes and abnormal appearance such as vessel haemorrhage, distortion and thickness can play a crucial role in glaucoma diagnosis [26]. The primary and most effected vascular portion in glaucomatous eye is the rim portion of OD. In the proposed method, only blood vessels of rim area are extracted from the entire OD portion. In rim vessel detection process first blood vessel segmentation has been performed by multilayered thresholding based blood vessel segmentation proposed in [27]. In this segmentation process, first vessel enhancement has been achieved using 2D Gabor wavelet then thresholding based vessel segmentation has been performed. The thin blood vessels along with thick ones have been extracted using multilayered thresholding. After blood vessel segmentation from the OD image, rim vessels have been further extracted by applying a rim mask on extracted OD vessels. Rim mask has been developed by already extracted cup and disc area. The following six features are further obtained from rim vessels:

(1) Total area covered by vessels map of NRR ($f_4$)
(2) Mean of the areas in the vessel map of NRR ($f_5$)
(3) Kurtosis of the distribution of areas of the vessels in the NRR ($f_6$)
(4) Standard deviation of the distribution of areas of the vessels in the NRR ($f_7$)
(5) Variance of the distribution of areas of the vessels in the NRR ($f_8$)
(6) Skew of the distribution of areas of the vessels in the NRR ($f_9$)

### 4.2 Grey level co-occurrence matrix (GLCM) ($f_{10}$–$f_{14}$)

The excavation caused by the decay of fibre nerves in OD of glaucoma eye can be captured using GLCM features. GLCM provides statistics about the relative location of the neighbourhood pixels in an image [28]. Let $P(i, j)$ is GLCM for an image $I$ of size $m \times n$. Following five GLCM features [29] are extracted and employed in the proposed system.

1. Contrast ($f_{10}$)

$$\mathrm{CT} = \sum_{n=0}^{G-1} n^2 \left\{ \sum_{i=1}^{G} \sum_{j=1}^{G} P(i, j) \right\}, \quad |i, j| = n \tag{4}$$

2. Entropy ($f_{11}$)

$$\mathrm{ET} = \sum_{i=0}^{G-1} \sum_{j=0}^{G-1} P(i, j) \times |\log(P(i, j)) \tag{5}$$

3. Correlation ($f_{12}$)

$$\mathrm{CR} = \sum_{i=0}^{G-1} \sum_{j=0}^{G-1} \frac{\{i \times j\} \times P(i, j) - \{\mu_x \times \mu_y\}}{\sigma_x \sigma_y} \tag{6}$$

4. Cluster shade ($f_{13}$)

$$\mathrm{CS} = \sum_{i=0}^{G-1} \sum_{j=0}^{G-1} \{i + j - \mu_x - \mu_y\}^3 \times P(i, j) \tag{7}$$

5. Energy ($f_{14}$)

$$\mathrm{EG} = \sum_{i=0}^{G-1} \sum_{j=0}^{G-1} (P(i, j))^2 \tag{8}$$

---

In above, $G$ denotes the number of grey levels used and $\mu_x$, $\sigma_x$, $\mu_y$, $\sigma_y$ are means and standard deviations of $P_x$ and $P_y$. $P_x(i)$ is the $i$th entry obtained by summing the rows of $P(i, j)$.

### 4.3 Discrete wavelet transform ($f_{14}$–$f_{54}$)

DWT can be used to extract both frequency and location information. Instead of obtaining global image features, it collects details in horizontal, vertical and diagonal orientations. The main purpose to use DWT as a texture feature in proposed solution is to capture changes which appear on OD to differentiate between normal and glaucoma cases. In the digital image, the smooth variations in colours are known as low-frequency variations, and sharp variations are termed as high-frequency variations. One way to isolate smooth variations and details from an image is by using DWT. This linear transformation functions on data vector with length of integer power of two. It isolates each data into distinct frequency modules and then studies each module with matching resolutions to its scale. The computation of DWT has been done with cascade of filtering followed by a factor 2 sub-sampling. Outputs of high- and low-pass filters have been given by [30]

$$a_{j+1}[P] = \sum_{n=-\infty}^{+\infty} l[n - 2p] aj[n] \tag{9}$$

$$d_{j+1}[P] = \sum_{n=-\infty}^{+\infty} h[n - 2p] aj[n] \tag{10}$$

where $aj$ subscript elements are used for next step of the transform and $d_j$ subscript element is wavelet coefficients, which finalise the transform output. $l[n]$ is the low-pass filter coefficient and $h[n]$ is the coefficient of high-pass filters. Supposing that scale $j + 1$ has half number of $a$ and $d$ elements than scale $j$ causes DWT to be done until only two $aj$ subscript elements known as scaling function coefficients left in signal to analyse. In the proposed system, $1 \times 20$ feature vector containing the first two moments of wavelet coefficients have been extracting using single-level discrete 2D wavelet transform. A total of 40 features are extracted using this approach.

### 4.4 Mean grey-level ($f_{55}$)

Cup is the brightest region in OD. In glaucoma eye because of widen cup, the mean grey-level of OD is found to be greater than normal eye. The mean grey-level of OD image has been computed by converting RGB image to grey scale followed by its mean calculation.

### 4.5 Grey-level run length ($f_{56}$–$f_{62}$)

A grey-level run is a collection of successive, collinear image pixels with similar grey level value. The element $p(i, j)$ of matrix states the count of a run of length $j$ with grey level $i$ in given direction [31]. In digital images with rough texture, grey-level runs are found to be longer than smooth texture images [32]. In normal eye relatively more grey-level runs are found due to rough texture as compared to glaucoma eye. In proposed method, seven texture features from the run-length matrix are extracted, and out of these seven features, five features introduced by Galloway [31] are as follows.

*4.5.1 Short runs emphasis ($f_{56}$):* In this function each run length value is divided by the length of the run squared

$$\mathrm{SRE} = \frac{1}{n_\mathrm{r}} \sum_{i=1}^{M} \sum_{j=1}^{N} \frac{P(i,j)}{j^2} = \frac{1}{n_\mathrm{r}} \sum_{j=1}^{N} \frac{P_r(j)}{j^2} \tag{11}$$

*4.5.2 Long runs emphasis ($f_{57}$):* In following function each run length value is multiplied by the length of the run squared

$$\mathrm{LRE} = \frac{1}{n_\mathrm{r}} \sum_{i=1}^{M} \sum_{j=1}^{N} P(i,j) - j^2 = \frac{1}{n_\mathrm{r}} \sum_{j=1}^{n} P_r(j) - j^2 \tag{12}$$

*4.5.3 Grey-level non-uniformity ($f_{58}$):* Following function first takes square of total number of run lengths for each grey level, and then obtained sum of the squares is divided by the normalising factor of the total number of runs in the image

$$\mathrm{GLN} = \frac{1}{n_\mathrm{r}} \sum_{i=1}^{M} \left( \sum_{j=1}^{N} P(i,j)^2 \right) = \frac{1}{n_\mathrm{r}} \sum_{j=1}^{N} P_g(i)^2 \tag{13}$$

*4.5.4 Run length non-uniformity (RLN) ($f_{59}$):* Following function takes square of the number of runs for each length, and then obtained sum of the squares is divided by the normalising factor

$$\mathrm{RLN} = \frac{1}{n_\mathrm{r}} \sum_{j=1}^{N} \left( \sum_{i=1}^{M} P(i,j)^2 \right) = \frac{1}{n_\mathrm{r}} \sum_{j=1}^{N} P_r(i)^2 \tag{14}$$

*4.5.5 Run percentage (RP) ($f_{60}$):* Following function is the percentage of the total number of runs to the total number of possible runs

$$\mathrm{RP} = \frac{n_\mathrm{r}}{n_\mathrm{p}} \tag{15}$$

Apart from these five basic grey-level run length matrix features, two additional features proposed by Chu *et al.* [33] are also involved in feature set. These two features are defined as follows.

$$\mathrm{LGRE} = \frac{1}{n_\mathrm{r}} \sum_{i=1}^{M} \sum_{j=1}^{N} \frac{P(i,j)}{i^2} = \frac{1}{n_\mathrm{r}} \sum_{j=1}^{N} \frac{P_g(i)}{i^2} \tag{16}$$

*4.5.7 High grey-level run emphasis (HGRE) ($f_{62}$):*

$$\mathrm{HGRE} = \frac{1}{n_\mathrm{r}} \sum_{i=1}^{M} \sum_{j=1}^{N} P(i,j) \cdot i^2 = \frac{1}{n_\mathrm{r}} \sum_{j=1}^{N} P_g(i) \cdot i^2 \tag{17}$$

where $n_\mathrm{r}$ and $n_\mathrm{p}$ are the total number of runs and total number of pixels in the image, respectively. Considering that most features are only functions of $P_r(j)$, without observing the grey-level information contained in $P_g(i)$.

### *4.6 Segmentation-based fractal texture analysis (SFTA) ($f_{62}$–$f_{110}$)*

Complexity of shape can be assessed and measured using fractal dimension. In normal eye, cup boundary is more irregular due to presence of large blood vessels as compared to glaucomatous eye OD (see Fig. 6). A proficient SFTA has been proposed in [24]. The SFTA algorithm consists of two main parts: first decomposition of the input image into groups of binary images using two-threshold binary decomposition (TTBD) algorithm. Next fractal dimension of each resultant binary image has been computed. The TTBD further consists of two main parts: first a set of thresholding values calculated using multi-level Otsu algorithm, second the grey-scale image $I(x, y)$ has been disintegrated into group of binary images by choosing pairs of threshold values from $T$ and two-threshold segmentation has been applied as follows:

$$I_\mathrm{b}(x,y) = \begin{cases} 1, & \text{if } t_l < I(x,y) \le t_u \\ 0, & \text{otherwise} \end{cases} \tag{18}$$

where $t_1$ is the lower threshold value and $t_\mathrm{u}$ is the upper threshold value. Similarly, the region boundaries $\Delta(x, y)$ of binary image $I_\mathrm{b}$ $(x, y)$ have been computed as follows:

$$\Delta(x,y) = \begin{cases} 1, & \text{if } \exists (x'-y') \in N_8[(x,y)] \\ & I_\mathrm{b}(x'-y') = 0 \wedge \\ & I_\mathrm{b}(x'-y') = 1 \\ 0, & \text{otherwise} \end{cases} \tag{19}$$

In above, $N_8$ [([$x$, $\underline{y}$])] is the group of eight-connected pixels to ($x$, $y$). If pixels at location ($x$, $y$) in resultant binary image $I\_\mathrm{b}$ ($x$, $y$) has 1 value and at least one of neighbourhood pixel with 0 value, then 1 value is assigned to $\Delta(x, y)$, else 0 value is assigned to $\Delta(x, y)$. The fractal dimension $D_0$ of each border image has been computed using (3).

In the proposed method, SFTA algorithm is used for texture analysis. It requires the user to set the parameter *nt* which defines the number of thresholds that will be employed in the input image decomposition. Algorithm returns a $6 * nt$ vector $\boldsymbol{D}$ mined from the input image. In our case $nt = 8$ has been used because it has given best results for classification, and 48 features have been extracted using SFTA algorithm.

### *4.7 Brightness ($f_{111}$)*

Glaucoma effected OD has overall more brightness due to the large size of the cup and less number of nerve fibres. RGB pixels have been converted to brightest values using the following equation[34]:

$$V = 0.299\mathrm{R} + 0.587\mathrm{G} + 0.114\mathrm{B} \tag{20}$$

Default weighted factors for RGB to YUV conversion have been used to compute brightness.

### *4.8 Colour moments ($f_{111}$–$f_{117}$)*

The enlarged cup in glaucomatous eye forms a smoother variation in colours as compared to normal eye. Colour moments can be used to obtain global image features unlike DWT. It can be used to measure colour similarities between images. In colour moments, the occurrence of a colour in an image is represented as a probability distribution function. First two colour moments mean and standard deviation has been used to analyse colour similarities in the proposed system. RGB colour image has been first decomposed into red, green and blue channels, then moment described in (21) and (22) have been calculated for each channel [35]. In our case, six colour moments have been computed by calculating first two moments of each channel

$$\text{Mean} = \frac{1}{N^2} \sum_{x=1}^{N} \sum_{y=1}^{N} f(x,y) \tag{21}$$

$$\text{Standard deviation} = \sqrt{\frac{1}{N^2} \sum_{x=1}^{N} \sum_{y=1}^{N} (f(x,y) - \mu)^2} \tag{22}$$

### *4.9 Super-pixels ($f_{118}$)*

In glaucoma eye OD, due to cup enlargement and degeneration of fibre, the numbers of super-pixels in the red channel of glaucoma eye OD are usually greater than the number of super-pixels in red channel of normal eye OD. In the proposed method, all pixels in the red channel of OD image are termed as super-pixels with pixel values larger than or equal to threshold $T = 0.9$. Following expression explains the thresholding strategy:

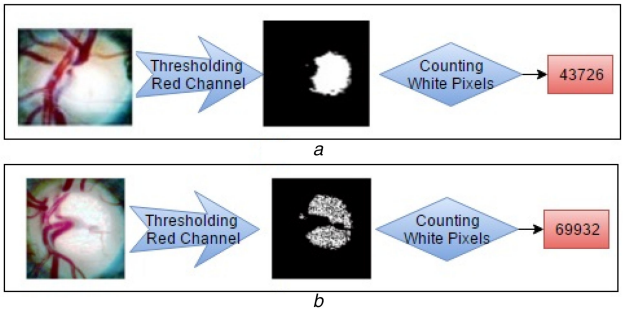


**Fig. 7** *Super-pixel calculation process and results of normal and glaucoma OD*
***(a)*** Super-pixels in normal OD, ***(b)*** Super-pixels in glaucoma OD

**Table 1** Comparison of isolated and hybrid texture features classification results

| | Accuracy | Specificity | Sensitivity |
|---|---|---|---|
| GLCM features | 84 | 83 | 85 |
| super-pixels | 63 | 35 | 94 |
| brightness | 56 | 27 | 88 |
| wavelet features | 91 | 92 | 90 |
| grey-level run length | 72 | 73 | 71 |
| mean grey level | 48 | 40 | 56 |
| colour moment | 76 | 69 | 83 |
| SFTA | 84 | 87 | 81 |
| rim-vessels features | 57 | 63 | 50 |
| wavelet features | 86 | 83 | 90 |
| grey-level run length mean grey level | | | |
| GLCM features | 62 | 48 | 77 |
| super-pixels | | | |
| brightness | | | |
| colour moment | 83 | 87 | 79 |
| SFTA rim-vessels features | | | |
| GLCM features | 70 | 83 | 56 |
| grey-level run length | | | |
| vertical RDR | | | |
| rim-vessels features | | | |
| SFTA | 90 | 88 | 92 |
| wavelet features | | | |
| brightness | | | |
| wavelet features | 81 | 79 | 83 |
| GLCM features | | | |
| super-pixels | | | |
| colour moment | 60 | 54 | 67 |
| brightness | | | |
| super-pixels grey | | | |
| grey-level run length | | | |
| HTF module (combined) | 94 | 92 | 96 |

**Table 2** Confusion matrix for HTF module

| | Healthy | Glaucoma |
|---|---|---|
| healthy | 48 | 4 |
| glaucoma | 2 | 46 |

$$g(x,y)=\begin{cases}1, & \text{if } f(x,y)\geq 0.9\\ 2, & \text{if } f(x,y)<0.9\end{cases} \tag{23}$$

After thresholding, all survived super-pixels in image $g(x,y)$ have been calculated. Figs. 7*a* and *b* shows super-pixel calculation process and results of normal and glaucoma OD, respectively. It can be noted that there is a considerable difference in the total number of super-pixels in normal and glaucoma OD.

## 5 Classification and grading

In the proposed system, classification is performed on HTF and HSF features separately and SVM has been used as classifier. SVM is famous for best handling of multi-dimensional data, binary classification and robustness added with help of different kernels [36]. In our case, we have used RBF as kernel along with SVM. Both modules use SVM independently and make a binary decision about glaucoma based on input feature vector. HSF module uses all features explained in Section 3 to classify input image as glaucoma or normal. Similarly, HTF module uses all features explained in Section 4 to make same decision. The proposed system then makes a final decision after correlating results of both the classifiers. The input image is labelled as glaucoma if both the modules categorise it as glaucomatous; similarly, if both the modules grade it as healthy then it is classified as healthy. However, if the results of both the modules do not match then it is considered as suspected.

## 6 Results

### 6.1 Datasets

The proposed system has been tested on publicly available glaucoma database (Glaucoma DB) consisting of 100 labelled images annotated by ophthalmologists with clinical CDR (CCDR) values, which are used as a benchmark for the computed CDR values [37]. Dataset consists of 52 normal and 48 glaucoma images captured using Top Con TRC 50EX camera with a resolution of $1504 \times 1000$.

### 6.2 Results

Performance analysis is done using sensitivity, specificity and accuracy as performance measures. The evaluation is first performed for HTF and HSF modules separately and then analysis of final result obtained by correlating results from both modules. Table 1 shows the evaluation of proposed system with different kind of features. Comparison between performance accuracy of isolated and combined feature for automated glaucoma detection can be made by analysing table data. The experiments have been conducted using ten-fold cross-validation technique and SVM classifier along with RBF is used. In case of sensitivity, proposed super-pixels feature outperforms others with sensitivity of 94%. Wavelet features showed best overall performance with 91% accuracy and 92% specificity. In the case of hybrid feature sets, different combinations of features have been analysed, but maximum accuracy is achieved by combining all isolated texture features.

Table 2 shows confusion matrix for HTF module, it has been able to detect 46 out of 48 glaucoma cases accurately and 48 out of 52 normal cases accurately. Concisely, HTF module has been able to identify 94 out of 100 cases correctly, i.e. 94% accuracy with 96% sensitivity and 92% specificity. Results of HTF module reveal that texture features can capture appearance-based changes and intensity variation caused by glaucoma and can be effectively used to achieve high sensitivity rate.

Similarly, a comparison of classification results of isolated and combined structural features has been conducted in Table 3. Results showed that in case of isolated structural features, CDR structural feature performed the best with 78% accuracy, but maximum accuracy has been gained by the grouping of all isolated structural features, i.e. the HSF module which achieved maximum accuracy of 83% with the maximum specificity of 88%.

Confusion matrix for HSF module is shown in Table 4. HSF module has been able to detect 37 out of 48 glaucoma cases and 46 out of 52 normal cases accurately. HSF module has been able to identify 83 out of 100 cases accurately with 77% sensitivity and 88% specificity.

A comparison of CDR and CCDR values has been made to analyse the performance of proposed CDR calculation method. Fig. 8 illustrates that the maximum deviation of computed CDR values from CCDR values is 0.37. Mean error of the proposed system has been 0.11. Fig 8 and Table 5 represent comparison of

**Table 3** Comparison of isolated and hybrid structural features classification results

| Technique | Accuracy | Specificity | Sensitivity |
|---|---|---|---|
| CDR | 78 | 83 | 73 |
| vertical RDR | 73 | 62 | 85 |
| cup boundary | 61 | 63 | 58 |
| CDR<br>cup boundary | 74 | 85 | 63 |
| CDR<br>vertical RDR | 52 | 10 | 98 |
| vertical RDR<br>cup boundary | 74 | 65 | 83 |
| HSF module (combined) | 83 | 88 | 77 |

**Table 4** Confusion matrix for HSF module

| | Healthy | Glaucoma |
|---|---|---|
| Healthy | 46 | 6 |
| Glaucoma | 11 | 37 |

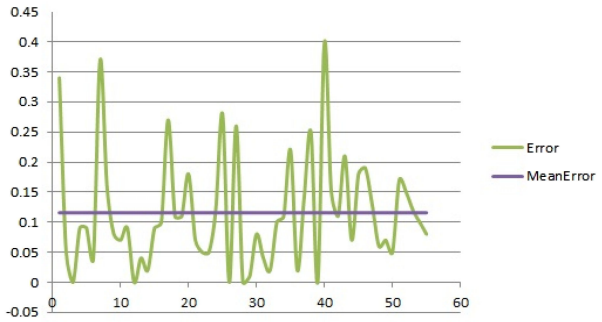


**Fig. 8**
*Error and mean error in CDR values compared with CCDR values*

**Table 6** Correlating results from HTF and HSF modules

| | Healthy | Glaucoma | Suspected |
|---|---|---|---|
| Healthy | 42 | 0 | 10 |
| Glaucoma | 0 | 35 | 13 |

**Table 5** CDR values computed by proposed methodology

| Image | CDR | CCDR | Image | CDR | CCDR | Image | CDR | CCDR |
|---|---|---|---|---|---|---|---|---|
| 1 | 0.74 | 0.4 | 20 | 0.42 | 0.6 | 39 | 0.5 | 0.5 |
| 2 | 0.45 | 0.4 | 21 | 0.53 | 0.6 | 40 | 0.8 | 0.4 |
| 3 | 0.75 | 0.75 | 22 | 0.45 | 0.5 | 41 | 0.45 | 0.3 |
| 4 | 0.51 | 0.6 | 23 | 0.5 | 0.45 | 42 | 0.49 | 0.6 |
| 5 | 0.61 | 0.7 | 24 | 0.52 | 0.4 | 43 | 0.39 | 0.6 |
| 6 | 0.44 | 0.4 | 25 | 0.52 | 0.8 | 44 | 0.47 | 0.4 |
| 7 | 0.67 | 0.3 | 26 | 0.5 | 0.5 | 45 | 0.58 | 0.4 |
| 8 | 0.46 | 0.3 | 27 | 0.66 | 0.4 | 46 | 0.51 | 0.7 |
| 9 | 0.48 | 0.4 | 28 | 0.5 | 0.5 | 47 | 0.43 | 0.3 |
| 10 | 0.47 | 0.4 | 29 | 0.49 | 0.5 | 48 | 0.44 | 0.5 |
| 11 | 0.51 | 0.6 | 30 | 0.48 | 0.4 | 49 | 0.53 | 0.6 |
| 12 | 0.5 | 0.5 | 31 | 0.51 | 0.55 | 50 | 0.55 | 0.5 |
| 13 | 0.46 | 0.5 | 32 | 0.48 | 0.5 | 51 | 0.47 | 0.3 |
| 14 | 0.52 | 0.5 | 33 | 0.4 | 0.5 | 52 | 0.6 | 0.75 |
| 15 | 0.51 | 0.6 | 34 | 0.41 | 0.3 | 53 | 0.58 | 0.7 |
| 16 | 0.6 | 0.7 | 35 | 0.58 | 0.8 | 54 | 0.38 | 0.48 |
| 17 | 0.57 | 0.3 | 36 | 0.78 | 0.8 | 55 | 0.32 | 0.4 |
| 18 | 0.39 | 0.5 | 37 | 0.54 | 0.4 | | | |
| 19 | 0.39 | 0.5 | 38 | 0.55 | 0.8 | | | |

CCDR values and CDR values of 55 randomly selected images from whole local database.

One of the novel contributions of proposed system is the inclusion of 'suspect' class in the decision. Here, results from HSF and HTF modules are correlated in a way that if results do not converge on a single decision, then they are classified as suspected. Patients classified as suspected, or glaucomatous, are referred to specialists for further detailed investigation. The confusion matrix with inclusion of suspect class is shown in Table 6. These results demonstrate that final CAD system after correlating results from both modules has generated outstanding and improved results with 100% accuracy for referral of glaucoma cases.

Enhanced performance of proposed system shown in Tables 1, 2 and 6 have outperformed the results presented in recent work of Akram *et al.* [37] and Khan *et al.* [6]. Algorithm in [6] was evaluated on a dataset of 50 images composed from MESSIDOR, HEI-MED, DRIVE, STARE and DiaRetDB0 publically available databases of fundus images. Whereas in [37] same database as used in proposed system has been used. Comparison of proposed CAD system with the algorithm in [6, 37] is shown in Table 7.

## 7 Discussion and conclusion

**Table 7** Comparison of results with already deployed techniques

| | Specificity, % | Sensitivity, % | Accuracy, % |
|---|---|---|---|
| proposed HSF module | 88 | 77 | 83 |
| proposed HTF module | 92 | 96 | 94 |
| glaucoma detection using hybrid feature set [37] | 92.9 | 87.5 | 90.84 |
| glaucoma detection using CDR and ISNT rule [6] | 85 | 73 | 82 |

The menace of glaucoma can be harnessed with the proposed versatile CAD system which outperforms its contemporary automated models in many ways. Existing methods mostly rely of CDR and few have used features along with classification for diagnosis of glaucoma. These methods suffer from low sensitivity due to presence of noise and other changes. In order to improve sensitivity, the proposed system has a unique combination of robust structural and textural features including a novel proposed super-pixels based feature. The combinations of structural and textural features in both modules have been finalised after a rigorous

analysis process. Primarily, performance of each feature has been analysed individually, results showed no redundant feature (Tables 1 and 3). Then, performances of several possible combinations of features have been tested. Texture features such as local binary patterns and autocorrelograms have been removed from HTF module because these features were reducing overall accuracy of system. Finally, the combinations of structural and textural features with maximum accuracy and best performance have been selected. The superior performance of proposed system also lies in the fact that we have utilised structural and textural information of optic nerve head. We have used two different channels for the cup analysis, i.e. blue channel for cup boundary calculation and red channel in the cases where illumination noise is present. In fundus images, the background colour tone varies from patient to patient. So even images acquired from same camera have different intensities [38] which affect the robustness of CAD systems. Threshold values and binary object (in our case disc and cup) sizes vary due to two main reasons, i.e. different spatial resolution and different intensities. In pre-processing step, both these issues have been addressed by scaling, enhancement and cropping of input image. These pre-processing methods also enable system to deal with the issues of images acquired from different cameras. Finally, the best empirically tested values for thresholding and size parameters for cup and disc segmentation are selected. We have applied texture analysis on red channel to capture intensity variations caused by glaucoma, and results have shown tremendous improvement. The proposed system also included a third decision class, i.e. suspect which helped in screening out glaucoma patients with 100% accuracy since not a single glaucoma case has been referred as normal. Hence, in rural areas where there is a scarcity of ophthalmologist, the proposed system can be used for glaucoma diagnosis and only genuine cases can be forwarded to the specialist for further examinations. Fundus image does not provide in depth analysis of optic nerve and it is being carried out using optical coherence tomography (OCT) images. In future we can use fundus and OCT image and fuse their analysis to get more accurate and reliable results for diagnosis of glaucoma.

## 8 References


[1] 'World Health Organization: Prevention of Blindness and Visual Impairment'. Available at http://www.who.int/blindness/causes/priority/en/, accessed April 2016

[2] Quigley, H.A., Broman, A.T.: 'The number of people with glaucoma worldwide in 2010 and 2020', *Br. J. Ophthalmol.*, 2006, **90**, (3), pp. 262–267

[3] 'Review of Ophthalmology: How to Evaluate the Suspicious Optic Disc'. Available at http://www.reviewofophthalmology.com/content/d/cover_focus/i/1315/c/25316/, accessed December 2015

[4] Cheng, J., Yin, F., Wong, D.W. K., *et al.*: 'Sparse dissimilarity-constrained coding for glaucoma screening', *IEEE Trans. Biomed. Eng.*, 2015, **62**, (5), pp. 1395–1403

[5] Dutta, M.K., Mourya, A.K., Singh, A., *et al.*: 'Glaucoma detection by segmenting the super pixels from fundus colour retinal images'. 2014 Int. Conf. on Medical Imaging, m-Health and Emerging Communication Systems (MedCom), Greater Noida, 2014, pp. 86–90

[6] Khan, F., Khan, S.A., Yasin, U.U., *et al.*: 'Detection of glaucoma using retinal fundus images'. The 6th 2013 Biomedical Engineering Int. Conf., Amphur Muang, 2013, pp. 1–5

[7] Agarwal, A., Gulia, S., Chaudhary, S., *et al.*: 'Automatic glaucoma detection using adaptive threshold based technique in fundus image'. 38th Int. Conf. on Telecommunications and Signal Processing (TSP), Prague, 2015, pp. 416–420

[8] Joshi, G.D., Sivaswamy, J., Krishnadas, S.R.: 'Optic disk and cup segmentation from monocular color retinal images for glaucoma assessment', *IEEE Trans. Med. Imaging*, 2011, **30**, (6), pp. 1192–1205

[9] Hatanaka, Y., Noudo, A., Muramatsu, C., *et al.*: 'Vertical cup-to-disk ratio measurement for diagnosis of glaucoma fundus images'. Proc. SPIE 7624, Medical Imaging 2010: Computer-Aided Diagnosis, 76243C, March 2010

[10] Acharya, U., Ng, E., Eugene, L., *et al.*: 'Decision support system for the glaucoma using Gabor transformation', *Biomed. Signal Proc. Control*, 2015, **15**, pp. 18–26

[11] Dua, S., Acharya, U.R., Chowriappa, P., *et al.*: 'Wavelet-based energy features for glaucomatous image classification', *IEEE Trans. Inf. Technol. Biomed.*, 2012, **16**, (1), pp. 80–87

[12] Deepak, K., Jain, M., Joshi, G., *et al.*: 'Motion pattern-based image features for glaucoma detection from retinal images'. Proc. of the Eighth Indian Conf. on Computer Vision, Graphics and Image Processing – ICVGIP '12, Mumbai, India, December 2012, article No. 47

[13] Bhatt, P., Patel, S., Shah, A., *et al.*: 'Image Enhancement Using Various Interpolation Methods', *Int. J. Comput. Sci. Inf. Technol. Secur.*, 2012, **2**, (4), pp. 799–803

[14] 'MathWorks: Crop an Image'. Available at http://www.mathworks.com/help/images/ref/imcrop.html, accessed February 2016

[15] 'Intensity Histogram'. Available at http://homepages.inf.ed.ac.uk/rbf/HIPR2/histgram.htm, accessed February 2016

[16] Willis, C.: 'Glaucoma in optometric practice: a survey of optometrists', *Ophthalmic Physiol. Opt.*, 2000, **20**, (1), pp. 70–75

[17] 'Morphological Image Processing'. Available at https://www.cs.auckland.ac.nz/courses/compsci773s1c/lectures/ImageProcessing-html/topic4.htm, accessed February 2016

[18] 'Maths Work: Bwareaopen'. Available at http://www.mathworks.com/help/images/ref/bwareaopen.html, accessed February 2016

[19] 'Maths Work: Regionprops'. Available at http://www.mathworks.com/help/images/ref/regionprops.html, accessed February 2016

[20] Spaeth, G.L.: 'Appearances of the optic disc in glaucoma: a pathogenetic classification'. Symp. on Glaucoma, Transactions of the New Orleans Academy of Ophthalmology, CV Mosby, St. Louis, 1981, pp. 114–152

[21] Spaeth, G.L., Lopes, F., Junk, A.K.: 'Systems for staging the amount of optic nerve damage in glaucoma: a critical review and new material', *Surv. Ophthalmol.*, 2006, **51**, (4), pp. 293–315

[22] Rangayyan, R.M., Nguyen, T.M.: 'Fractal analysis of contours of breast masses in mammograms', *J. Digit. Imaging*, 2007, **20**, (3), pp. 223–237

[23] Lamani, D., Manjunath, T.C., Ramegowda, : 'Fractal dimension with object rotation: a case study with glaucoma eye'. 2014 Fifth Int. Conf. on Signal and Image Processing, Jeju Island, 2014, pp. 111–116

[24] Costa, A.F., Humpire-Mamani, G., Traina, M.: 'An efficient algorithm for fractal analysis of textures'. 25th SIBGRAPI Conf. on Graphics, Patterns and Images, Ouro Preto, 2012, pp. 39–46

[25] 'Microvascular Changes Might Predict Glaucoma'. Medpagetoday.com, http://www.medpagetoday.com/ophthalmology/glaucoma/36692, accessed March 2017

[26] Ho, C.Y., Pai, T.W., Chang, H.T., *et al.*: 'An atomatic fundus image analysis system for clinical diagnosis of glaucoma'. 2011 Int. Conf. on Complex, Intelligent, and Software Intensive Systems, Seoul, 2011, pp. 559–564

[27] Akram, M., Khan, S.: 'Multilayered thresholding-based blood vessel segmentation for screening of diabetic retinopathy', *Eng. Comput.*, 2012, **29**, (2), pp. 165–173

[28] Eleyan, A., Demirel, H.: 'Co-occurrence based statistical approach for face recognition'. 2009 24th Int. Symp. on Computer and Information Sciences, Guzelyurt, 2009, pp. 611–615

[29] Nitish, Z., Vrushsen, P.: 'GLCM textural features for brain tumor classification', *IJCSI Int. J. Comput. Sci. Issues*, 2012, **9**, (3), pp. 354–359

[30] Kociołek, M., Materka, A., Strzelecki, M.: 'Discrete wavelet transform – derived features for digital image texture analysis'. Proc. of Int. Conf. on Signals and Electronic Systems, Lodz, Poland, September 2001, pp. 163–168

[31] Galloway, M.: 'Texture analysis using gray level run lengths', *Comput. Graph. Image Process.*, 1975, **4**, (2), pp. 172–179

[32] Xiaoou, T.: 'Texture information in run-length matrices', *IEEE Trans. Image Process.*, 1998, **7**, (11), pp. 1602–1609

[33] Chu, A., Sehgal, C., Greenleaf, J.: 'Use of gray value distribution of run lengths for texture analysis', *Pattern Recognit. Lett.*, 1990, **11**, (6), pp. 415–419

[34] 'Analyze Menu'. Available at http://rsb.info.nih.gov/ij/docs/menus/analyze.html, accessed April 2016

[35] 'Colour Moments'. Available at http://homepages.inf.ed.ac.uk/rbf/CVonline/LOCAL_COPIES/AV0405/KEEN/av_as2_nkeen.pdf, accessed April 2016

[36] Kotsiantis, S.B.: 'Supervised machine learning: a review of classification techniques', *Informatica*, 2007, **31**, pp. 249–268

[37] Akram, M., Tariq, A., Khalid, S., *et al.*: 'Glaucoma detection using novel optic disc localization, hybrid feature set and classification techniques', *Australas. Phys. Eng. Sci. Med.*, 2015, **38**, (4), pp. 643–655

[38] Bourne, R.: 'Ethnicity and ocular imaging', *Eye*, 2010, **25**, (3), pp. 297–300